Real-time Sub-nanogram Resolution Measurement of Inertial Mass and Density Using Magnetic-field Guided Bubble Microthruster

Leilei Wang,[1#] Minjia Sheng,[2#] Fengchang Yang,[1,3] Lina Wang,[2] Hangyu Li,[1,3] Pengcheng Nie,[1,3] Dongshi Guan,[1,3] Xiaohuan Wang,[1] Long Li,[1] Li Chen,[2] Anthony L. Hu,[4] Haihang Cui[2*], and Xu Zheng,[1*]

1 State Key Laboratory of Nonlinear Mechanics, Beijing Key Laboratory of Engineered Construction and Mechanobiology, Institute of Mechanics, Chinese Academy of Sciences, Beijing 100190, China

2 School of Building Services Science and Engineering, Xi'an University of Architecture and Technology, Xi'an 710055, China

3 School of Engineering Science, University of Chinese Academy of Sciences, Beijing 100049, China

4 The High School Affiliated to Renmin University of China, Beijing 100080, China

# L. W. and M. S, contributed equally to this work.

* Corresponding Authors:

Xu Zheng: zhengxu@lnm.imech.ac.cn, orcid.org/0000-0002-2398-9283

Haihang Cui: cuihaihang@xauat.edu.cn

Abstract:

Artificial micro/nanomotors utilizing active particles exhibit enormous potential in applications such as drug delivery and microfabrication. However, their substantial upgrade to micro/nanorobots capable of executing precise tasks with sophisticated functions remains a significant challenge. In this paper, we develop a bubble microthruster (BMT) – a new variation on the bubble driven microrobot – that focuses energy from a collapsed microbubble to create a hydrodynamic jet to exert inertial impact on nearby micro-objects. Benefiting from the easy magnetic-field guided control via gamepad, the BMT can perform real-time measurements on designated micro-objects with the assistance of high-speed imaging. By measuring the transient response of the micro-object and fitting the relaxation time, the inertial mass and density of micro-objects can be determined. Our study validates our approach by measuring the mass of polystyrene microparticles and the effective density of hollow glass microspheres, and unravel a sub-nanogram resolution that could be suitable to detect variation in mass or density of cells or embryos. The BMT technique illuminates the development of a chip-free method for biological microparticles, integrating with manipulation using microrobot and detection of physical properties. This technique may provide versatility and simplicity in complex environments compared to current methods using cantilever/resonator in microfluidic chips.

Keyword: Bubble Microthruster, Real-time sub-nanogram resolution measurement, Magnetic manipulation, Hydrodynamic jet flow, Biological particle.

1. Introduction

The emerging technique of artificial micro/nano-motors[1, 2] provides a vivid example of the idea using tiny machines to finish jobs in microscopic world, first proposed by Richard Feynman in his famous speech "There's plenty of room at the bottom"[3]. These micro/nano-motors can harvest energy from ambient environment by means of chemical reaction[4-6] and other external fields (like acoustic[7, 8], magnetic fields[9-14], light[15, 16], etc.), and manifest autonomous movements. Integrated with manipulation strategies based on hydrodynamics and external field steering, micro/nano-machine or micro/nano-robot have been recently developed to serve various applications, such as targeted drug delivery[17-20], minimally invasive surgery[21].

Among many micro/nano-motors, microbubble driven micromotor is a unique type that can reach the highest propulsion speed[4, 22], owing to the high surface energy of the bubble and the focused hydrodynamic jet during bubble collapse[4, 22] that can significantly enhance micromotor's propulsion. Recent progress has demonstrated that the microbubble itself can implement new functions for the micromotor based on bubble dynamics and induced hydrodynamic flow[4], rather than merely providing energy. For instance, bubble microrobot has been developed to realize functions like gripper, pusher, and anchor, which shows high maneuverability and easy switch of different speeds and functions[4]. The bubble microrobot can be applied as a key manipulation tool in microfabrication platform at the air-liquid interface for two-dimensional soft functionalized film or micro electronic[11].

In fact, more functions can be extracted from the sophisticated mechanisms when microbubble is involved. Specifically, microbubble collapse and its induced hydrodynamic impact provide a transient inertial effect which is precious in microscopic world. Reminiscent of the scallop theorem[23], such inertial effect is desired to break time-reversal reciprocal motion in viscous low Reynolds number (Re number is defined as a ratio of inertial effect to viscous effect) flow for designing artificial microswimmers[5]. More importantly, the inertial effect offers a possibility to detect physical quantities in microscale, which is closely related to inertia but very difficult to measure by existing methods. For example, measuring the mass and mass variation of a living cell with size about 5 μm, which requires a sensitivity of approximately 100 pg = 10^{-10} g, could provide quantitative information linked to cell growth/death, composition variation, and response to drug treatments[24-26]. Compared with previous measurement methods based on nano resonator[26-32] or Raman scattering microscopy[25], bubble micromotor or microrobot could provide an alternative approach probing the mass or density of a tiny particle by its response to inertial impact, with merits like controllable single particle selection, easy manipulation, and real-time measurements.

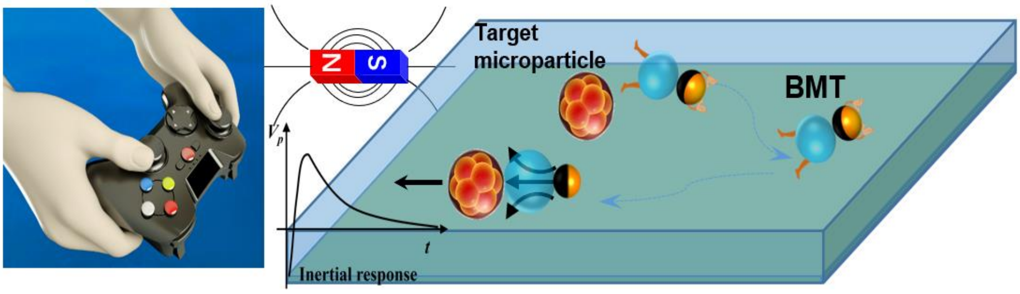

Fig. 1 Schematic diagram of the magnetic-field guided BMT, which can be easily controlled by a gamepad. The BMTG focuses the energy of the collapsed microbubble to impact the target microparticle and obtains the inertial mass and density of microparticle by measuring its inertial response to the impact.

Therefore, in this work we will show a novel concept using a controllable bubble microthruster (BMT) to measure the inertial mass and density of a tiny particle with sub-nanogram resolution. This magnetic-field guided BMT, which is easily manipulated using a gamepad, can exert inertial impact and focus hydrodynamic jet flow from microbubble's collapse to a target microparticle. The kinematic response of the target particle, which is recorded by a high speed camara (see Materials and Methods for detail), will be analyzed based on our theoretical model. The inertial mass and density can be measured by determining the relaxation time τ, which characterizes the transient movement of the target particle. In the following, we will explain the principle of the BMT, and demonstrate its validity and reliability based on results of microparticles with controlled sizes and densities. The BMT is further applied to measure densities of different biological particles, including cells (like hela, hepatocyte, nephrocyte) and embryos.

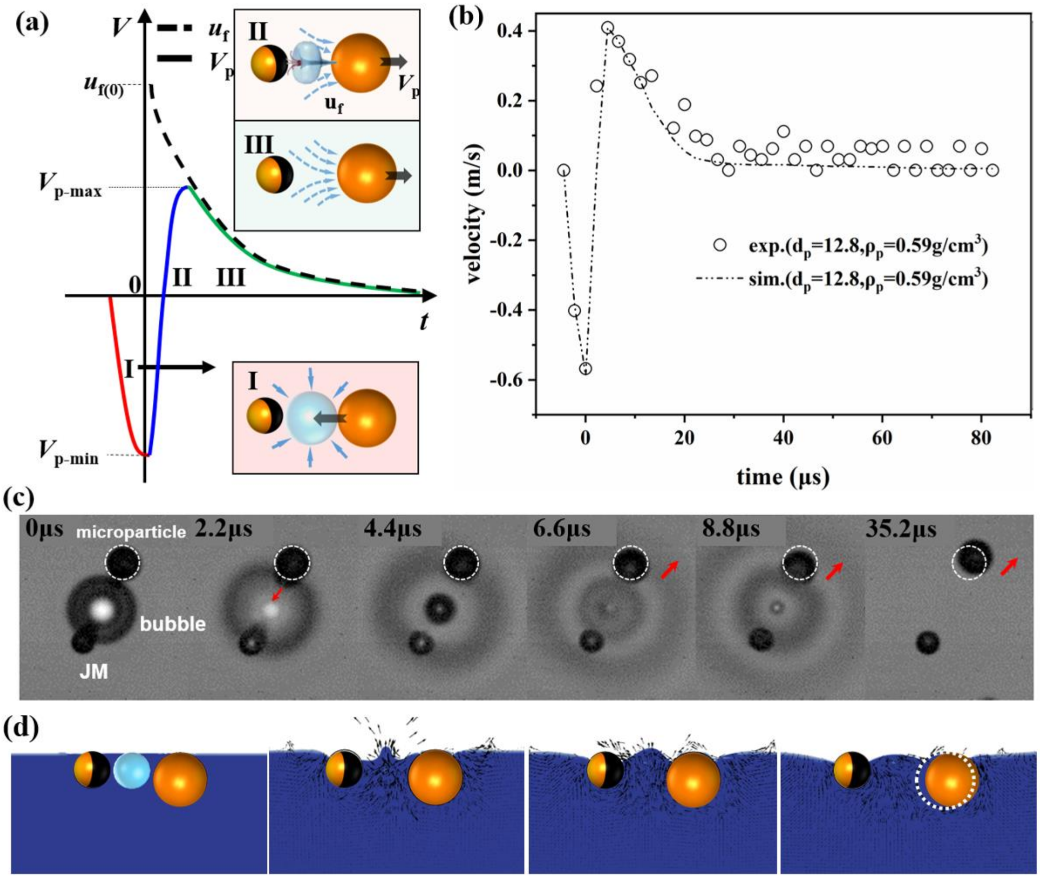

Fig. 2 The principle of the inertial mass measurement is based on the transient velocity variation of the target particle as a response to the inertial impact from the bubble collapse. (a) Diagram of a 3-stage velocity variation V_p of the target microparticle. In stage I (red) the particle withdraws to the bubble cavity after the bubble collapse. In stage II (blue) the transient hydrodynamic flow exerts a strong propulsion to the particle and changes the particle's velocity to positive. In stage III (green) after the particle reaches its maximum speed it will slow down with the flow of surrounding fluid. The dashed curve illustrates the decay of the velocity of ambient fluid u_f. (b) The measured velocity variation in stage II and III of a microparticle (radius R_p = 6.4 μm, density ρ_p = 0.59 g/cm^3) by a high speed camara. The measured data is compared with the dashed curve obtained from numerical simulation, showing a good agreement. (c) Snapshots of the BMT from experiment during bubble collapse. The white circles represent the initial position of target microparticle. (d) Snapshots from numerical simulation showing the flow field and the motion of the microparticle at t = 0 μs, 5 μs, 10 μs, 50 μs, respectively. The white dotted circle in the last snapshot displays the original position of the microparticle.

2. Principle of Inertial Mass/Density Measurement

In the experiment, we used a gamepad to guide the BMT's approaching to the target microparticle (Fig. 1, SM video S1). The BMT's translational motion is propelled by the catalytic on the platinum surface of the Janus micromotor (JM); whereas its orientation and steering are controlled by a magnetic field generated by a 3D Helmhotz electromagnetic coil (HEC) system (SM)[4]. After approaching, a JM-bubble-particle configuration is established by turning bubble in the middle. Hydrodynamic theory and simulation[4] have predicted a strong hydrodynamic jet flow caused by bubble collapse. The direction of this jet flow is determined by the surrounding confinement: in this JM-bubble-particle configuration the flow will point to the side with stronger confinement depending on the size. As illustrated in Fig. 2(a), the BMT is suitable to work when the JM's diameter is smaller than that of the target particle, which is called a "pusher mode" [4] as the jet flow will push the target particle away from its original position.

The transient response of the target microparticle pushed by the BMT is the key to measure the inertial mass/density, which can be divided into three stages as shown in Fig. 2(a). In stage I (red curve) right after the bubble collapse, the microparticle withdraws to the cavity of the bubble dragged by the flow of the surrounding fluid. The hydrodynamic jet flow towards the particle will instantaneously form after the fluid has filled the bubble cavity, which rapidly turn the particle's velocity V_p from negative to positive in stage II (blue curve). Stage III begins when the particle's speed reaches its maximum value, which equals to the fluid speed u_f (dashed curve in Fig. 2(a)). In stage III (green curve), the particle's speed V_p will decrease gradually accompanying the decay of the surrounding flow $u_f(t)$ due to viscous dissipation.

This 3-stage velocity variation is verified by our experiment using a microparticle with radius R_p = 6.4 μm, observed by a high speed camara (450, 000 frame per second), as shown in Fig. 2(b) and experimental snapshots in Fig. 2(c). We can see that stage II is a very rapid process only lasting approximately 4.8 μs respectively, while stage 3 takes a much longer time exceeding 50 μs. Note that the duration of bubble collapse is known to be $0.5\tau_R \approx 3.9$ μs ($\tau_R = \sqrt{\rho {R_b}^3/\gamma}$ is the inertial Rayleigh timescale, which is calculated to be 7.8 μs in this case when R_b = 16.1 μm for the bubble)[33, 34], which is in good agreement with the 4.8 μs duration observed in our experiment. We also perform numerical simulation to show the transient flow field during bubble collapse (Fig. 2d), which provides valuable information for analyzing the hydrodynamic drag force exerted on the target particle. In the simulation, the sizes of the JM, the bubble and the microparticle are 20 μm, 20 μm, and 35 μm, respectively. The simulation flow field supports the above illustration of the working principle, and the propelled displacement of the microparticle shown in Fig. 2(d) within 50 μs is approximately 7.6 μm, in agreement with experimental observation, In addition, the *Re* number reaches 5 based on the maximum speed of the particle approximately 0.4 m/s, clearly indicating the transient inertial effect introduced by the BM during the above process.

We then establish a kinematic equation for the particle's transient motion in stage II and stage III:

$$m_p \frac{dV_p}{dt} = 6\pi\mu R_p [u_f(t) - V_p] \qquad (1)$$

where m_p and R_p are the inertial mass and radius of the target microparticle, and μ is fluid viscosity. It is known that the relaxation time $\tau_p = 2R_p^2\rho_p/9\mu$ is the key parameter in this kind of kinematic equation, characterizing the typical time of the temporal variation of the inertial response $V_p(t)$. To tackle the difficulty of solving eq. (1) due to the complex flow field $u_f(t)$, we propose an approach to solve the microparticle velocity $V_p(t)$. According to our experimental observation showing a rapid and a slow decay of $u_f(t)$ in stage III respectively, we introduce an equation consisting of two exponential parts to model the variation of the fluid velocity $u_f(t)$:

$$u_f(t) = (c_1 e^{-t/\tau_1} + c_2 e^{-t/\tau_2}) \qquad (2)$$

where τ_1 and τ_2 are the typical timescales of the rapid and slow fluid velocity decay respectively in stage III, and the parameters c_1 and c_2 are determined by the initial velocity as $u_f(0) = c_1 + c_2$. As discussed in Fig. 2(b), the rapid dynamics is characterized by the Rayleigh timescale, and we find $\tau_1 = 0.5\,\tau_R$. The slow decay follows a much longer timescale τ_2, which is approximately 100 μs determined by the long-tail of the experimental data in the range of t = 30 – 100 μs. Substituting eq. (2) into (1), we can fully solve the first-order ordinary differential equation with initial condition $V_p(0)$ obtained from the experimental observation of the largest negative velocity at $t = 0$.

$$V_p(t) = e^{-t/\tau_p}[\frac{c_1\tau_1}{\tau_1-\tau_p}e^{(t/\tau_p-t/\tau_1)} + \frac{c_2\tau_2}{\tau_2-\tau_p}e^{(t/\tau_p-t/\tau_2)}] + Ce^{-t/\tau_p} \quad (3)$$

Obvious, the parameter C is closely related to the initial condition, *i.e.*, $C = V_p(0) - (\frac{c_1\tau_1}{\tau_1-\tau_p} + \frac{c_2\tau_2}{\tau_2-\tau_p})$. In eq. (3), there are only two unknown parameters obtained by fitting experimental data: the relaxation time of target microparticle τ_p, and the initial fluid velocity $u_f(0)$. The microparticle's density ρ_p is calculated by $\rho_p = 9\mu\tau_p/2R_p^2$, and the inertial mass is obtained by multiplying the volume of microparticle with ρ_p.

3. Working Regime of BMT

A critical issue hindering the functioning of the BMT is that in certain circumstance bubble collapse could cause withdrawal of target particle rather than propelling it. Briefly, the hydrodynamic mechanism is significantly influenced by the asymmetric confinement from the JM and the target microparticle on both sides of the bubble. After a JM-bubble-particle combination is formed following the gamepad manipulation, the bubble collapse will introduce a hydrodynamic jet flow towards the side of stronger confinement (as demonstrated in Fig. 2 and our previous study[4]). If the target microparticle is larger than the JM, the hydrodynamic jet flow will point to the microparticle forming a "pusher" mode, which is referred to as bubble microthruster or BMT in this study. On the contrary, if the JM is larger than the target particle, a "puller" mode is formed which drags the particle back to the bubble. It is interesting to mentioned that a "anchor" mode will form if the sizes of JM and particle are identical.

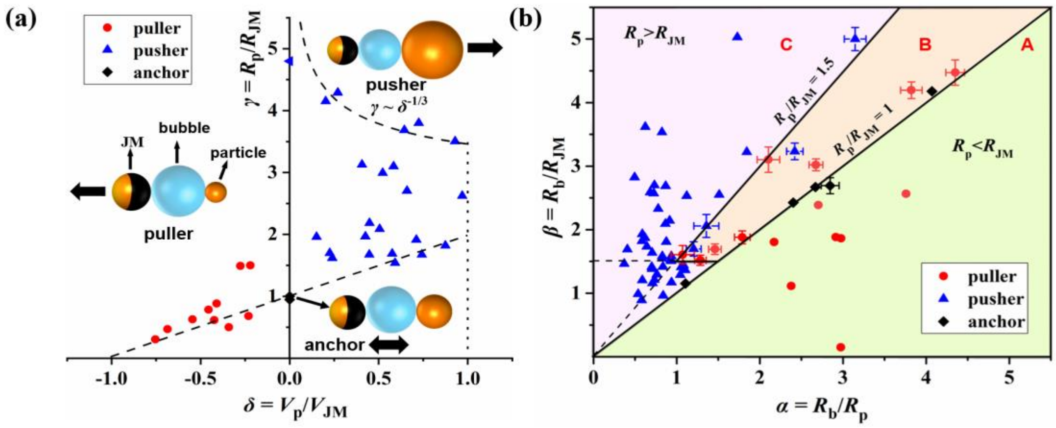

Fig. 3 Distinguishing two basic working modes of the BMT: pusher vs. puller. (a) A phase diagram based on the particle-to-JM size ratio γ vs. the velocity ratio δ. And (b) a phase diagram based on the bubble-to-JM size ratio β vs. the bubble-to-particle size ratio α.

Notably, the working modes depend on the size ratios and the velocity ratios between the JM and the target microparticle. Fig. 3 shows two phase diagrams of different working modes, *i.e.*, pusher, puller and anchor, based on four dimensionless parameters: $\alpha = R_b/R_p$, $\beta = R_b/R_{JM}$, $\gamma = R_p/R_{JM}$, and $\delta = \overline{V_p}/\overline{V_{JM}}$, where R_b, R_p, and R_{JM} are the radii of the bubble, the microparticle, and the JM, respectively, $\overline{V_p}$ is the average velocity of the microparticle in a bubble cycle, and $\overline{V_{JM}}$ is the average velocity of the JM without loading the microparticle. Fig. 3(a) distinguishes the working modes based on the microparticle-to-JM size ratio γ vs. the velocity ratio δ. The value $\gamma = 1$ indicates a symmetric system around the bubble, which results in no net displacement of the microparticle in a full bubble cycle. The reciprocal motions of both microparticle and JM around the bubble form the "anchor" mode with $\overline{V_p} = 0$ and $\delta = 0$ (black diamond) in Fig. 3(a), as illustrated in our previous work [4].

When $0<\gamma<1$, the hydrodynamic jet flow will point to the JM and drag the microparticle back to the JM side, resulting in a "puller" mode with $\delta < 0$ (red circles in Fig. 3(a)). When the size of the microparticle is much smaller than the JM, the particle will follow JM completely. When $\gamma>1$, the hydrodynamic jet flow will point to the target particle forming a "pusher" mode with $\delta > 0$ (blue triangles in Fig. 3(a)), which is needed to realize the function of BMT. In our experiments, we find that to form a stable pusher mode the value of γ should exceed 1.5 rather than the ideal value 1. In addition, we show the upper and lower boundaries (dashed curves) of all the experimental data in the phase diagram in Fig. 3(a). The lower boundary approximately passes through (-1, 0) and (0, 1) in the δ - γ coordinates. And the upper boundary obeys a scaling of $\gamma \sim \delta^{1/3}$, which is governed by the law of conservation of momentum (SM).

Another phase diagram can be obtained by taking the bubble effect into account, as shown in Fig. 3(b). The two axes are defined based on the bubble-to-JM size ratio β vs. the bubble-to-particle size ratio α. We obtained regime A, *i.e.*, the lower right part of the slope R_p/R_{JM}=1, which is a purely puller mode, and regime C, *i.e.*, the upper left part of the slope R_p/R_{JM}=1.5, which is a purely pusher mode. An intermediate regime B is located at 1< R_p/R_{JM}<1.5, in which stable pusher mode is achieved when approximately $\beta = R_b/R_{JM} < 1.5$. This puller mode above the threshold value β =1.5 can be attributed to the clear withdrawal of the microparticle to the bubble cavity if the bubble is too big.

4. Implementations

Based on the results shown in Fig. 3, we can precisely control the BMT to work in the pusher mode as long as the primary condition $\gamma > 1.5$ is fulfilled. To avoid disturbance from large bubble and insufficient energy of small bubble, β is chosen to be $1 < \beta < 2.5$ in the experiments shown below. It is important to stress that the smallest JM used in our experiments was approximately R_{JM} = 3.4 μm, because bubble might not appear on smaller JM's surface due to higher free energy barrier for bubble nucleation.[4] Based on the threshold $\gamma > 1.5$, the smallest target microparticles is approximately R_p = 5.1 μm, whose mass is approximately 0.55 ng if its density is assumed to be 1 g/cm^3. Assuming a 20% measurement uncertainty, our method is able to reach a mass resolution approximately 0.1 ng (which will be discussed later).

To verify the effectiveness of the BMT, we will first use polystyrene (PS) microspheres with different sizes and fixed density ρ = 1.05 g/cm^3 as target microparticles. The measured sizes using our BMT method are in good agreement with the values obtained by microscopic observation. Further, we will use hollow glass microspheres (HGMs) with adjustable densities to show that the BMT can solve more difficult task. In addition, the BMT is applied to measure mass and density of different cells and embryos, demonstrating the feasibility of using BMT as a real-time, convenient, and high-resolution method for probing mass/density variation of biological particles during different processes.

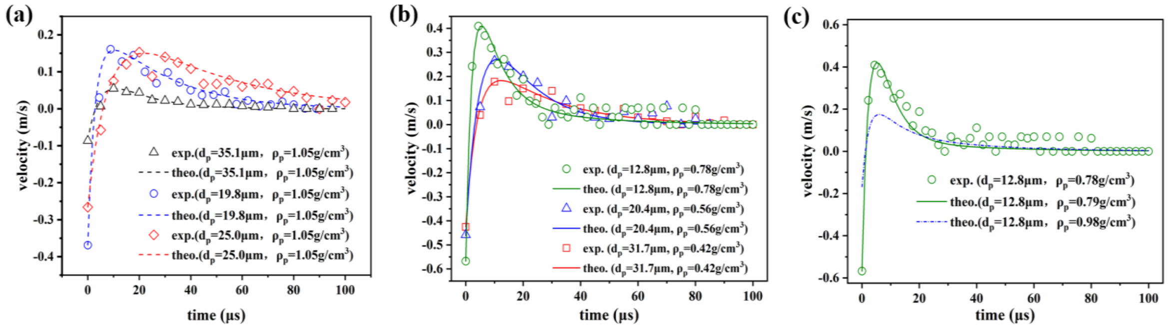

Fig. 4 The measured transient velocity variations compared with their fitted curves based on eq. (3). (a) Results using PS microspheres with fixed densities and different sizes. (b) Results using HGMs with different sizes and effective densities. (c) Results using HGMs coated with 40 nm platinum layer to adjust their effective densities.

4.1 Verification using PS microspheres with different sizes

We first verify the BMT method using PS microspheres with different sizes. As the density of PS microspheres is known to be approximately 1.05 g/cm^3, this measurement can demonstrate the validity of the BMT method. Fig. 4(a) shows the results using three different PS microspheres with measured diameters d_p = 19.8 μm, 25.0 μm, and 32.7 μm, respectively. The diameters of these PS microspheres were also examined using optical microscope with an objective of 100x/NA=1.4, which were found to be $d_{p\text{-}m}$ = 21.6 μm, 26.4 μm, and 33.5 μm, respectively. The deviations are only 9.0%, 5.6%, and 2.5% respectively, well verifying the BMT method. It is of interest to mention that the measured data d_p from BMT method are usually smaller than the values from optical microscope, which might be due to the influence of the free liquid-air surface. Our experiments are usually performed near the liquid-air surface due to the presence of bubbles. The theory based on eq. (3) may underestimate the size and mass of the target microparticles, because the microparticle could experience slightly lower drag force near the free surface.

4.2 Measuring density variation of HGMs

We then applied the BMT method to detect the effective density of HGMs. The HGMs consist of a glass shell (ρ_{shell} = 2.4 g/cm^3 and thickness $h \approx$ 1.2 μm measured by SEM) and a air cavity. Thus, the effective density of the HGMs is decreased with the increasing of the

HGMs' size, which can be characterized before the current BMT measurement (see SM for details). We first measured the effective density of HGMs with different sizes, as shown in Fig. 4(b). The fit based on eq. (3) shows that the effective density of a HGM with diameter d_p = 12.8 μm is approximately ρ_p = 0.89 g/cm^3, which is in good agreement with the value given in SM. For larger HGM (d_p = 31.7 μm), the effective density decreases to approximately ρ_p = 0.46 g/cm^3.

It is interesting to mention that we can easily adjust the mass/density of the HGMs by coating a nanoscale platinum (Pt) layer. For instance, by coating a 40 nm thick Pt layer, the effective density of the HGMs can be increased around 20%. We also measure the effective density of the coated HGMs with similar sizes, as shown in Fig. 4(c). The measured results show good sensitivity of the BMT method about the added mass of the coating, and the measured values are consistent with our prediction.

4.3 Measurement of Biological particle

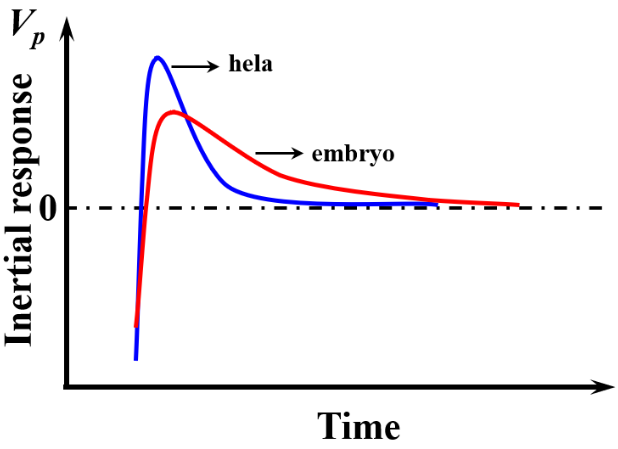

Fig. 5 The measured velocity variation of a single Hela cell (blue) and an embryo (red). The solid curves are the fit based on eq. (3). As the embryo is much larger than the Hela cell, its velocity peak due to the impact from the BMT is lower while its duration is broader.

To demonstrate the feasibility of the BMT method in wide applications, we try to measure the density of various microscale biological particles, such as cells and embryos. It was proposed that the density of cells could provide quantitative information linked to cell growth/death, composition variation, and response to drug treatments, however, few data have been reported. The BMT method should work in the pusher mode, which requires a larger size of the cell compared with the JM, therefore we start from Hela cell. The measured data and the fit curve based on eq. (3) are shown in Fig. 5. From the average value of 5 independent measurements, we estimated that the density of Hela cell is approximately 1.21±0.08 g/cm^3.

Except for cells, we also apply the BMT method to detect the density of a blastocyst, which is an early stage of embryo. A blastocyst usually consists of an outer TE layer, a cluster of inter cells, and a cavity, whose diameter is approximately 56.3 μm. Therefore, the density of the blastocyst should vary accompanying the dividing of inter cells and the expansion of the cavity during growth. We show a measured curve of a blastocyst in Fig. 5 (red), by which we obtained an effective density of the blastocyst ρ=1.05±0.08 g/cm^3. Due to the existence of the cavity, the effective density of the blastocyst is smaller than that of Hela cell.

4.4 Resolution

It is important to clarify the measurement resolution of the BMT method. Taking HGM with measured d_p = 12.8 μm and ρ_p = 0.59 g/cm^3 as an example, we show the fit curve (green solid line) and the upper and lower boundary of the fitting (red and blue dash-dotted curve respectively) in Fig. 6. Fig. 6(a) shows that the BMT method has a good size resolution which could be smaller than δd_p = 1.0 μm, manifesting a relative deviation smaller than 7.8%. The high size resolution is attributed to the leading term R_p^2 in the relaxation time $\tau_p = 2R_p^2\rho_p/9\mu$. Besides, the BMT method shows an acceptable resolution of density in Fig. 6(b), in which the measured result ρ_p = 0.59±0.08 g/cm^3 indicates a resolution of 0.08 g/cm^3. It is clear to see that the resolution of the BMT method is mainly determined by the positive peak of the measured velocity. Thus, for larger target microparticle, the resolution could be enhanced as the experiment obtain more data in the peak region resulting in a better fit. Nonetheless, large JM and bubble are also need to increase the peak value of the velocity.

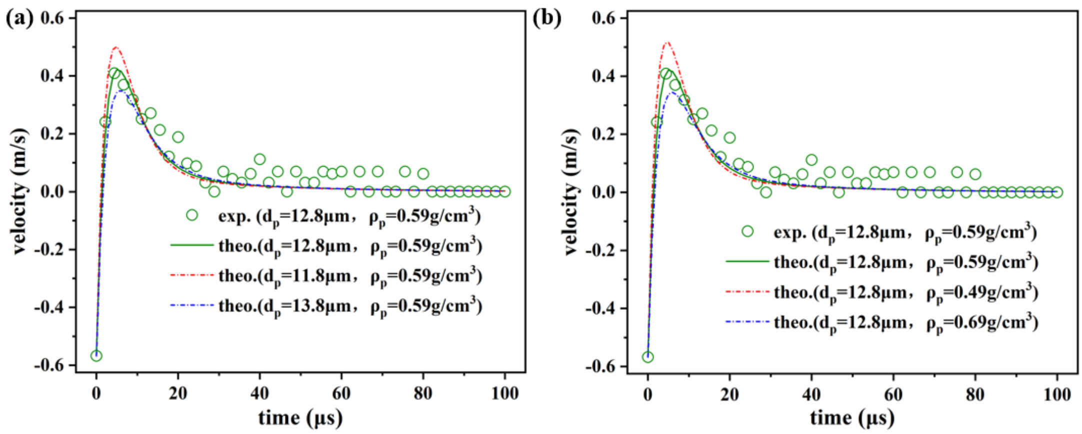

Fig. 6 The measurement resolution of (a) size and (b) density.

5. Conclusion

In summary, we show the BMT as a novel technique to achieve sub-nanogram resolution of measuring microparticle's inertial mass and density. The BMT focuses energy from a collapsed microbubble and exerts the inertial impact to an adjacent microparticle via a hydrodynamic jet. Integrated with magnetic field guided manipulation, the BMT can be easily controlled using a gamepad, which greatly promotes its maneuverability. By measuring the transient velocity variation of the microparticle under such inertial impact and fit it with a solution from the ordinary differential kinematic equation, we can determine the relaxation time τ_p and thus obtain the mass and density of the microparticle. We have demonstrated the validity and effectiveness of the BMT method using PS microspheres and HGMs with different sizes and densities. The measured results shows that the measured resolution of mass could be up to approximately 0.1 ng, and the resolution of density could be up to approximately 0.08 g/cm^3. The BMT method is further applied to different cells and embryos, showing the feasibility of being used for unconventional biological microparticles. We want to highlight that the BMT method provides a chip-free, real-time, convenient, and high precision approach to detect the mass/density of various microparticles. In particular, the applying of BMT method to monitor the density variation of cells might pave a new way for detecting cell growth/death, composition variation, and response to drug treatments.

Material and Method

Fabrication of Janus Microsphere: The hollow magnetic Janus micromotors were fabricated by coating Ni (~40 nm) and Pt (~ 20 nm) layers successively on the hemispheres of hollow glass microspheres (HGMs). The HGMs (diameter approximately 10-60 μm) were purchased from Sino-steel Co. Ltd, and the main component is SiO_2. HGMs of different particle size distribution could be obtained through screening and floatation. During fabrication, the dilute solution of the HGMs was uniformly spread on a hydrophilic polished silicon wafer and dried at 60°C to form a monolayer of HGMs on the silicon wafer. Then, a Ni layer with thickness of ~ 40 nm and a Pt layer with thickness of ~ 20 nm were successively evaporated on the surface of HGMs using an electron beam evaporator. Due to the compact arrangement of the HGMs, the Ni and Pt layers only covered the top hemispheres of the HGMs.

Magnetic manipulation system: We established a system for magnetic actuation. The magnetic field setup consisted of a computer, a gamepad, two signal generator, three power amplifier and a set of three-axial Helmholtz electromagnetic coil (HEC) equipped on the inverted optical microscope (Nikon Eclipse Ti-U). The output signal from the signal generator is amplified by the power amplifier. The amplified signal is used to drive a set of HEC, which generate a uniform magnetic field in arbitrary direction. Herein, we achieve the flexible adjustment of magnetic field direction through a gamepad with various self-defined programmed functions, and the signal generator is controlled by the gamepad to generate predetermined signals. The programming language is C++, the controller programming interface is Windows Multimedia Joystick API, and the serial port (RS-232 standard interface) programming interface is based on System. IO. Ports provide by NET Framework 4.0. More details can be found in text S2 in the Supplementary Information.

Experimental observation and analysis: The self-propulsion of the BM was observed under an inverted microscope (Nikon Eclipse Ti-U) equipped with a high-speed camera (Phantom v2512 and TMX 7510). The HEC system was equipped at the microscope platform to provide a three-dimensional magnetic field for the control of the microrobot. The objective lens is ×10 or ×20, and the frame frequency of the high-speed camera is up to 450,000 fps. The concentration of H_2O_2 is approximately from 3 – 5 % (v/v). The experimental movies were analyzed with movie Spot Tracker and ImageJ.

Supporting Materials

This Supporting Information is available free of charge at http://

Experimental materials and methods, details of numerical simulation are provided in the SM.

Notes

The authors declare no competing financial interest.

ACKNOWLEDGMENTS

The authors acknowledge the National Natural Science Foundation of China (Grant Nos. 12072350, 11972351, 12302357, and 11832017), the National Key R&D Program of China (2022YFF0503504, 2021YFA0719302), the China Postdoctoral Science Foundation (287749), Key Research and Development Program of Shaanxi Province (2021ZDLSF05-04), CAS Henan Industrial Technology Innovation & Incubation Center (2024151), and Natural Science Basic Research Plan in Shaanxi Province (2020JM-479).

References

[1] Barbara Mazzolai, Federico Carpi, Koichi Suzumori, Matteo Cianchetti, Thomas Speck, Stoyan K. Smoukov, Ingo Burgert, Tobias Keplinger, Gilberto Siqueira, Felix Vanneste, Olivier Goury, Christian Duriez, Thrishantha Nanayakkara, Bram Vanderborght, Joost Brancart, Seppe Terryn, Steven Rich, Ruiyuan Liu, Kenjiro Fukuda, Takao Someya, Marcello Calisti, Cecilia Laschi, Wenguang Sun, Gang Wang, Li Wen, Robert Baines, Sree Kalyan Patiballa, Rebecca Kramer, Daniela Rus, Peer Fischer, Friedrich Simmel, Andreas Lendlein, Roadmap on soft robotics: multifunctionality, adaptability and growth without borders, *Multifunctional Materials* 2022.

[2] B. Wang, K. Kostarelos, B. J. Nelson, L. Zhang, Trends in Micro-/Nanorobotics: Materials Development, Actuation, Localization, and System Integration for Biomedical Applications, *Adv Mater* 33(4) 2021, e2002047.

[3] Richard P. Feynman, There's plenty of room at the bottom, 1959.

[4] L. Wang, L. Chen, X. Zheng, Z. Yu, W. Lv, M. Sheng, L. Wang, P. Nie, H. Li, D. Guan, H. Cui, Multimodal Bubble Microrobot Near an Air-Water Interface, *Small* 18(39) 2022, e2203872.

[5] L. L. Wang, L. Chen, J. Zhang, J. M. Duan, L. Wang, Z. H. Silber-Li, X. Zheng, H. H. Cui, Efficient Propulsion and Hovering of Bubble-Driven Hollow Micromotors underneath an Air-Liquid Interface, *Langmuir* 34(35) 2018, 10426-10433.

[6] Y. S. Lin, X. G. Geng, Q. J. Chi, C. L. Wang, Z. Wang, Driving Forces of the Bubble-Driven Tubular Micromotor Based on the Full Life-Cycle of the Bubble, *Micromachines* 10(6) 2019, 415.

[7] L. Q. Ren, N. Nama, J. M. McNeill, F. Soto, Z. F. Yan, W. Liu, W. Wang, J. Wang, T. E. Mallouk, 3D steerable, acoustically powered microswimmers for single-particle manipulation, *Science Advances* 5(10) 2019, eaax3084.
[8] Z. G. Wu, L. Li, Y. R. Yang, P. Hu, Y. Li, S. Y. O. Yang, L. V. Wang, W. Gao, A microrobotic system guided by photoacoustic computed tomography for targeted navigation in intestines in vivo, *Science Robotics* 4(32) 2019, eaax0613.
[9] A. Ghosh, P. Fischer, Controlled Propulsion of Artificial Magnetic Nanostructured Propellers, *Nano Letters* 9(6) 2009, 2243-2245.
[10] T. Li, J. Li, K. I. Morozov, Z. Wu, T. Xu, I. Rozen, A. M. Leshansky, L. Li, J. Wang, Highly Efficient Freestyle Magnetic Nanoswimmer, *Nano Lett* 17(8) 2017, 5092-5098.
[11] A. Barbot, H. J. Tan, M. Power, F. Seichepine, G. Z. Yang, Floating magnetic microrobots for fiber functionalization, *Science Robotics* 4(34) 2019, eaax8336.
[12] J. F. Yu, D. D. Jin, K. F. Chan, Q. Q. Wang, K. Yuan, L. Zhang, Active generation and magnetic actuation of microrobotic swarms in bio-fluids, *Nature Communications* 10 2019.
[13] J. J. Abbott, E. Diller, A. J. Petruska, Magnetic Methods in Robotics, *Annual Review of Control, Robotics, and Autonomous Systems, Vol 3, 2020* 3 2020, 57-90.
[14] Nafiseh Ebrahimi, Chenghao Bi, David J. Cappelleri, Gastone Ciuti, Andrew T. Conn, Damien Faivre, Neda Habibi, Alexander Hošovský, Veronica Iacovacci, Islam S. M. Khalil, Veronika Magdanz, Sarthak Misra, Chytra Pawashe, Rasoul Rashidifar, Paul Eduardo David Soto-Rodriguez, Zoltan Fekete, Amir Jafari, Magnetic Actuation Methods in Bio/Soft Robotics, *Advanced Functional Materials* 31(11) 2020.
[15] J. Tong, D. Wang, Y. Liu, X. Lou, J. Jiang, B. Dong, R. Dong, M. Yang, Bioinspired micro/nanomotor with visible light energy-dependent forward, reverse, reciprocating, and spinning schooling motion, *Proc Natl Acad Sci U S A* 118(42) 2021, e2104481118.
[16] A. Sen, Self-propelled motors: Light-seeking synthetic trees, *Nature Nanotechnology* 11(12) 2016, 1003-1004.
[17] W. Gao, J. Wang, Synthetic micro/nanomotors in drug delivery, *Nanoscale* 6(18) 2014, 10486-10494.
[18] B. E. de Avila, P. Angsantikul, J. Li, M. Angel Lopez-Ramirez, D. E. Ramirez-Herrera, S. Thamphiwatana, C. Chen, J. Delezuk, R. Samakapiruk, V. Ramez, M. Obonyo, L. Zhang, J. Wang, Micromotor-enabled active drug delivery for in vivo treatment of stomach infection, *Nat Commun* 8(1) 2017, 272.
[19] M. Luo, Y. Z. Feng, T. W. Wang, J. G. Guan, Micro-/Nanorobots at Work in Active Drug Delivery, *Advanced Functional Materials* 28(25) 2018.
[20] S. Tang, F. Zhang, H. Gong, F. Wei, J. Zhuang, E. Karshalev, B. Esteban-Fernández de Ávila, C. Huang, Z. Zhou, Z. Li, L. Yin, H. Dong, R. H. Fang, X. Zhang, L. Zhang, J. Wang, Enzyme-powered Janus platelet cell robots for active and targeted drug delivery, *Science Robotics* 5(43) 2020.
[21] J. Li, B. Esteban-Fernández de Ávila, W. Gao, L. Zhang, J. Wang, Micro/Nanorobots for Biomedicine: Delivery, Surgery, Sensing, and Detoxification, *Science Robotics* 2(4) 2017.
[22] Y. Feng, D. Jia, H. Yue, J. Wang, W. Song, L. Li, A. M. Zhang, S. Li, X. Chang, D. Zhou, Breaking through Barriers: Ultrafast Microbullet Based on Cavitation Bubble, *Small* 2023, e2207565.
[23] E. M. Purcell, Life at low Reynolds number, *American Journal of Physics* 45(1) 1977, 3-11.

[24] D. Martinez-Martin, G. Flaschner, B. Gaub, S. Martin, R. Newton, C. Beerli, J. Mercer, C. Gerber, D. J. Muller, Inertial picobalance reveals fast mass fluctuations in mammalian cells, *Nature* 550(7677) 2017, 500-+.
[25] S. Oh, C. Lee, W. L. Yang, A. Li, A. Mukherjee, M. Basan, C. Z. Ran, W. Yin, C. J. Tabin, D. Fu, X. S. Xie, M. W. Kirschner, Protein and lipid mass concentration measurement in tissues by stimulated Raman scattering microscopy, *Proceedings of the National Academy of Sciences of the United States of America* 119(17) 2022.
[26] T. A. Zangle, M. A. Teitell, Live-cell mass profiling: an emerging approach in quantitative biophysics, *Nature Methods* 11(12) 2014, 1221-1228.
[27] T. P. Burg, M. Godin, S. M. Knudsen, W. Shen, G. Carlson, J. S. Foster, K. Babcock, S. R. Manalis, Weighing of biomolecules, single cells and single nanoparticles in fluid, *Nature* 446(7139) 2007, 1066-1069.
[28] K. Jensen, K. Kim, A. Zettl, An atomic-resolution nanomechanical mass sensor, *Nature Nanotechnology* 3(9) 2008, 533-537.
[29] W. H. Grover, A. K. Bryan, M. Diez-Silva, S. Suresh, J. M. Higgins, S. R. Manalis, Measuring single-cell density, *Proceedings of the National Academy of Sciences of the United States of America* 108(27) 2011, 10992-10996.
[30] A. K. Bryan, V. C. Hecht, W. J. Shen, K. Payer, W. H. Grover, S. R. Manalis, Measuring single cell mass, volume, and density with dual suspended microchannel resonators, *Lab on a Chip* 14(3) 2014, 569-576.
[31] S. Olcum, N. Cermak, S. C. Wasserman, K. S. Christine, H. Atsumi, K. R. Payer, W. J. Shen, J. C. Lee, A. M. Belcher, S. N. Bhatia, S. R. Manalis, Weighing nanoparticles in solution at the attogram scale, *Proceedings of the National Academy of Sciences of the United States of America* 111(4) 2014, 1310-1315.
[32] M. Gagino, G. Katsikis, S. Olcum, L. Virot, M. Cochet, A. Thuaire, S. R. Manalis, V. Agache, Suspended Nanochannel Resonator Arrays with Piezoresistive Sensors for High-Throughput Weighing of Nanoparticles in Solution, *Acs Sensors* 5(4) 2020, 1230-1238.
[33] A. M. Ganan-Calvo, Revision of Bubble Bursting: Universal Scaling Laws of Top Jet Drop Size and Speed, *Phys Rev Lett* 119(20) 2017, 204502.
[34] C. Y. Lai, J. Eggers, L. Deike, Bubble Bursting: Universal Cavity and Jet Profiles, *Phys Rev Lett* 121(14) 2018, 144501.